Biomedical Engineering Letters (2022) 12:19–35
https://doi.org/10.1007/s13534-021-00214-8

REVIEW ARTICLE

# Practical review on photoacoustic computed tomography using curved ultrasound array transducer

**Jinge Yang[1] · Seongwook Choi[1] · Chulhong Kim[1]**

Received: 30 September 2021 / Revised: 15 November 2021 / Accepted: 5 December 2021 / Published online: 19 December 2021


## Abstract

Photoacoustic computed tomography (PACT) has become a promising imaging modality from laboratory to clinical research. Of many components of PACT system, the ultrasound (US) array transducer is an essential device to simultaneously receive photoacoustic (PA) signals from several directions in a parallel manner. Many research groups and companies have developed various types of US array transducers while accounting the properties of the PA waves to achieve better image quality, deeper imaging depth, faster imaging speed, and a wider field of view. In this review, we present the implementation and application of the state-of-the-art PACT systems using several types of curved US arrays: arc-shaped, ring-shaped, and hemispherical array transducers. Furthermore, we discuss the current limitations of PACT and also potential future directions for enhancing them.

**Keywords** Photoacoustics · Optoacoustics · Medical imaging · Preclinical systems · Clinical systems · Ultrasound array transducer

## 1 Introduction

Photoacoustic imaging (PAI), also referred to as optoacoustic imaging (OAI), has become a rapidly growing biomedical imaging modality for the laboratory to clinical research [1–7]. The PAI reconstructs images from the ultrasound (US) signals generated from tissues when illuminated by a laser pulse due to the photoacoustic (PA) effect, where absorbed optical energy is converted into acoustic energy [8]. This inherent hybrid imaging modality, where optical excitation is combined with ultrasonic detection, offers several advantages: (1) PAI is a noninvasive and nonionizing modality [9]; (2) The acoustic scattering in tissue is much less (about three orders of magnitude) than optical scattering. Thus, PAI makes it possible to have high resolution images of deep tissue [2]; (3) PAI provides a multitude of tissue information including structural, functional, metabolic, kinetic, and histologic through endogenous contrast (e.g., hemoglobin, lipid, DNA/RNA, water, etc.) [8]; (4) Various exogenous contrast agents, such as nanoparticles and optical contrast agents, can also be used in PAI for molecular and cellular imaging [10]; (5) PAI provides speckle-free images [11]; (6) PAI is complementary to as well as compatible with other imaging modalities, especially optical imaging and US imaging [8].

Generally, there are two major implementations of PAI: photoacoustic computed tomography (PACT) and photoacoustic microscopy (PAM) [1, 2, 6, 12–15]. The PAM targets shallow tissue with two subtypes: acoustic resolution PAM (AR-PAM) which use high-frequency US transducer and weakly focused light to acquire images [16]. The other subtype, optical-resolution PAM (OR-PAM) uses focused laser beam and high-frequency US transducer [6, 17–27]. In contrast to PAM, the PACT targets deep tissues. High pulsed energy is used to illuminate the entire region of interest (ROI) and a transducer with high sensitivity and large directivity is then used to receive PA signals over the whole area [8, 28–32]. Since PACT allows deep-tissue imaging,

Jinge Yang and Seongwook Choi have contributed equally to this work.

✉ Chulhong Kim
chulhong@postech.edu

[1] Department of Electrical Engineering, Convergence IT Engineering, Mechanical Engineering, School of Interdisciplinary Bioscience and Bioengineering, and Medical Device Innovation Center, Pohang University of Science and Technology (POSTECH), 77 Cheongam-ro, Nam-gu, Pohang, Gyeongbuk, Republic of Korea

it is suitable for whole-body animal studies and has been widely used in preclinical and clinical applications [33, 34].

Of many significant components in the PACT system, the US array transducer is one of the major components and largely affects image quality. Based on the principle of PACT, the PA pressure wave $p(r,t)$ at position $r$ and time $t$ in an acoustically homogeneous and lossless medium in response to a heat function $H(r,t)$ obeys the following wave equation [14, 35]:

$$\nabla^2 p(r,t) - \frac{1}{v_s^2}\frac{\partial^2 p(r,t)}{\partial t^2} = -\frac{\Gamma}{v_s^2}\frac{\partial}{\partial t}H(r,t) \quad (1)$$

where $v_s$ is the speed of sound in the medium and $\Gamma$ is the Grüneisen parameter. When the laser light meet the heat-confinement and stress-confinement conditions [2], Heat function can be expressed as:

$$H(r,t) = H_s(r)\delta(t),$$

where $H_s(r) = \mu_a(r)\phi(r)$, $\mu_a(r)$ is the absorption coefficient and $\phi(r)$ is the optical fluence. The solution to Eq. (1) is then given by:

$$p(r,t) = \frac{1}{4\pi v_s}\frac{\partial}{\partial t}\int_{S'(t)}\frac{p_0(r')}{|r-r'|}dS'(t) \quad (2)$$

where $p_0(r') = \Gamma \times H_s(r')$ is the initial PA pressure.$S'(t)$ is a spherical surface centered at $r$ with a radius $|r - r'| = v_s t$. This equation indicates that in an acoustically homogeneous medium, the PA pressure $p$ at a spatial point $r$ and at time $t$ is proportional to the time derivative of the integral of the absorbed laser energy over the 3D spherical surface (a circle in the 2-D case) centered at $r$ and with a radius of $v_s t$ [35]. Thus, in the ideal situation, PA signals are detected along a whole circle ($2\pi$ radians) in the 2D case or sphere ($4\pi$ steradians) in the 3D case. The linear array transducers can be easily integrated with the clinical US platform [36–54], but the linear US array transducer has a finite aperture and bandwidth [33], which leads to radial artifacts and morphological distortions due to the limited detecting views of each element [4, 6]. To overcome this limitation, curved array transducers, including arc-shaped [55–68], ring-shaped [69–73], and hemispherical array have been developed (Fig. 1) [74–78]. In the 2D case, arc-shaped array transducer with over 60% bandwidth can cover a larger angle of view (~ 172°) compared to the linear transducer to give better image quality and are less affected by directional sensitivity (Fig. 1a). The ring-shaped array transducers can cover full $2\pi$ radians in the 2D case and are ideal for 2D PACT (Fig. 1b). However, PA waves in the elevational direction can't be captured when arc-shaped and ring-shaped arrays are used due to limited receiving angle of each element. To cover the PA waves through a spherical surface in the 3D case, hemispherical array transducers have been developed

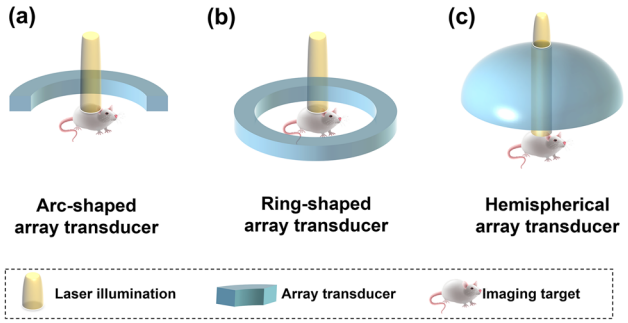


**Fig. 1** Three implementations of the PACT systems use (**a**) an arc-shaped array transducer, (**b**) a ring-shaped array transducer, and (**c**) a hemispherical array transducer. TR, transducer

(Fig. 1c). It receives 3D omnidirectional PA signals and thus generates the best quality 3D PACT volumetric images over the entire illuminated volume in real time.

This review focuses on three types of curved array transducers optimized for the PACT systems: arc-shaped, ring-shaped, and hemispherical array transducers. It avoids overlapping with recent review articles on PACT [6, 7, 15, 79–85]. We will also discuss the limitations of each type of array and summarize new types of transducers, which have been applied or have the potential to be used for the PACT system in the future.

## 2 PACT systems based on arc-shaped array transducers

Arc-shaped arrays utilize the directivity of elements to receive signals and overcome the limited-view artifacts of linear arrays to some extent [4]. Aiming at rapid and high-resolution tomographic imaging of small animals, Gamelin et al. developed a PACT system (Fig. 2a i) [55, 56] based on a 128-element curved US array transducer with 5 MHz central frequency, 80% bandwidth, and shaped to a quarter circle of 25 mm radius (Imasonic Inc., France). A Q-switched Nd:YAG laser pumped Ti: Sapphire laser (Symphotics Tii, LS-2134, Belarus) was used to deliver laser pulses, and it has a pulse-repetition frequency (PRF) of 15 Hz and the tunable wavelength range from 700 to 950 nm. The laser beam is diverged with a concave lens and homogenized by a circular profile engineered diffuser (ED1-S20, Thorlabs, USA) to produce a uniform illumination on the sample. They used the 16-channel data acquisition (DAQ) system and multiplexed with an 8:1 ratio, thus could obtain 128-channel data in total with eight laser pulses. The PA images were reconstructed using delay-and-sum or backprojection algorithm [35]. They achieved capture of a 90° field of view (FOV) image in less than one second and a complete 360° scanning within 15 s. During the experiment, the sample

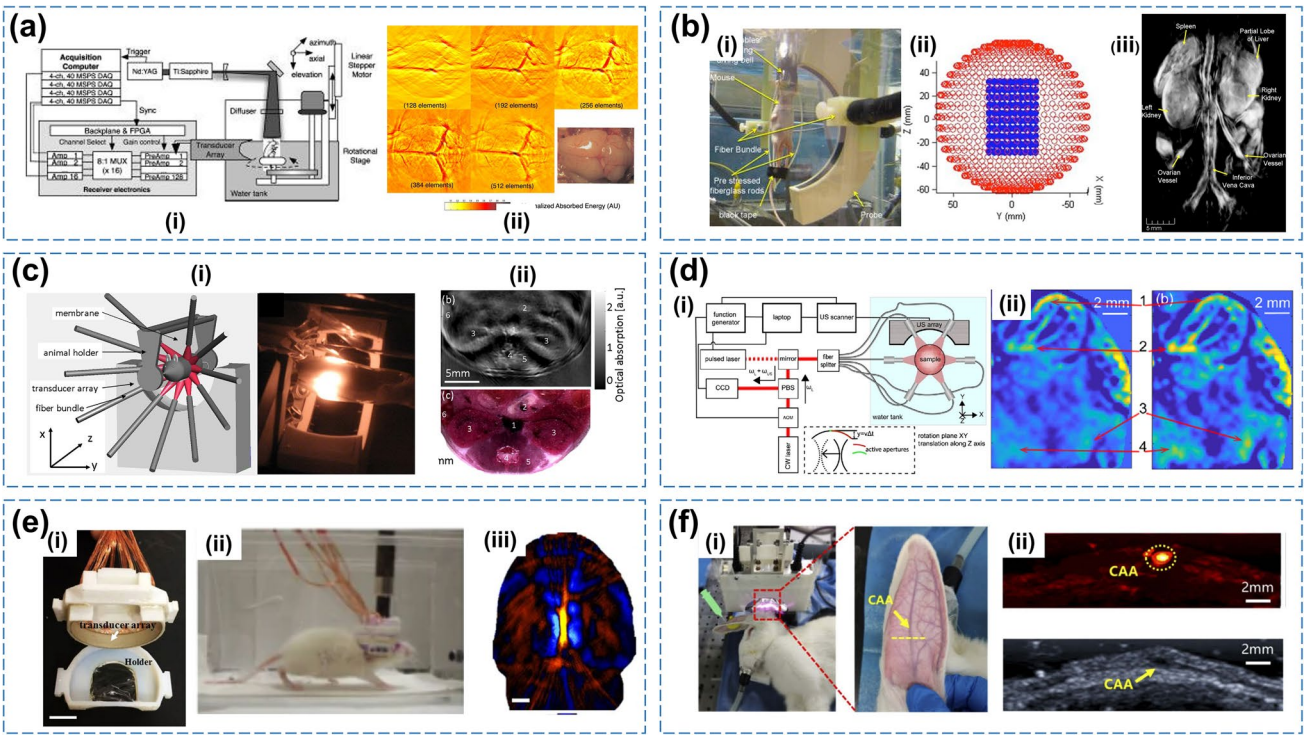


**Fig. 2** **a** (i) Schematic of the curved array based photoacoustic system [55, 56]. (ii) Ex vivo images of mouse brain in axial view with varying apertures. **b** (i)Picture of the spherical view PACT setup during a scan [57]. (ii) Side view of the reconstruction sphere showing the detector locations during one full rotation scanning. (iii) 3D photoacoustic image of a nude mouse. **c** (i) Schematic drawing of the array transducer, illumination device, and animal holder of MSOT system[58]. (ii) Cross-sectional cryslice and photoacoustic image of a nude mouse's abdomen. **d** (i) Illustration of photoacoustic and acousto-optic tomography system [59]. (ii) Before (left) and after (right) fluence-normalized photoacoustic (PA) images of a sacrificed mouse's cross-section. AOM, acousto-optic modulator; PBS, polarization beam splitter; CCD, charged-coupled device. **e** (i) Photograph of the miniature 3D wearable PACT system [60]. (ii) Photograph to show the behaving ability of a rat while wearing the developed system. (iii) Total cerebral hemoglobin PA image in a behaving rat. **f** (i) Photographs of in vivo imaging setup of the rabbit ear [61]. (ii) PA (above) and ultrasound (bottom) images of the rabbit ear. All images were reproduced with permission from. [55–61]

was mounted on a rotary stage positioned at the center of curvature. The in-plane resolution of this system was about 200 µm and the imaging depth for the phantom test was greater than 3 cm. They obtained ex vivo PA images of the mouse brain's vasculature (Fig. 2a ii).

The Brecht et al. developed a spherical view PACT system capable of in vivo whole-body imaging using an arc-shaped array transducer [57]. The array has a 65 mm radius of curvature, 64 elements, 3.1 MHz central frequency, and greater than 80% bandwidth (Imasonic Inc., France) (Fig. 2b i). An alexandrite laser (755 nm, 100 mJ output energy, 75 ns pulse width, 10 Hz PRF; Somerset, USA) and an Nd:YAG laser (1064 nm, 100 mJ output energy, 15 ns pulse width, 10 Hz PRF; Quantel, France) were used to support light illumination. The animal was illuminated orthogonally to the array with two wide beams of light originating from a bifurcated fiber bundle (Fig. 2b i). The animal was mounted on a custom-made mouse holder consisting of two hollow cylinders connected with fiberglass rods. The target was rotated 360° in 150 steps within a sphere for tomographic imaging, as shown in Fig. 2bii. Data were acquired from 9600 virtual transducer elements placed on the sphere and were used to form a three-dimensional (3D) tomographic image using a 3D-reconstruction algorithm. The system could generate high-quality PA images of individual organs and blood vessels throughout the mouse's whole body with a spatial resolution of about 0.5 mm and a field of view of 40 mm × 40 mm × 60 mm (Fig. 2b iii). The acquisition time for the full 360° scan was 8 min using an average of 32 laser pulses.

Razansky et al. [58] developed a whole-body multi-spectral optoacoustic tomography (MSOT) with a custom-made arc-shaped array transducer (Fig. 2c i). This arc-shaped array had 64 elements with 5 MHz central frequency and over 50% bandwidth (Imasonic Inc., France) and covered an angle of 172° around the target. The excitation light from a tunable optical parametric oscillator laser (680–950 nm; Opotek Inc., USA) with 10 ns pulse width and 10 Hz PRF was guided into a fiber bundle (CeramOptec, Germany). The ten arms were positioned evenly around the animal to create a

ring-shaped illumination around the mouse body coinciding with the US detection plane. The PA signals were received by eight multi-channel analog-to-digital system (Model PXI-5105, National Instruments, USA). Animals were held inside a water-impenetrable membrane positioned in the center of the imaging system. For obtaining a whole-body image, a linear stage (NRT150, Thorlabs, USA) was used to allow linear translation of the animal holder. The image was reconstructed based on the interpolated-matrix-model inversion method. The system could render cross-sectional reconstructions in real-time with an in-plane resolution of 150 µm and in-elevation resolution of 800 µm. They obtained a single-wavelength PA image of the mouse abdomen and identified the spine (1), kidneys (2), spleen (3), and vena cava (4) (Fig. 2c ii).

In the following few years, this MSOT system was improved with a 270° arc-shaped array transducer to cover larger angles around the object for enhancing image quality [86]. A fast wavelength tuning laser with up to 100 Hz PRF was also applied [87]. They also combined US imaging system with MSOT for a dual modality [88] and obtained the whole-body image of the animal by scanning the array along the elevation dimension. Based on those technologies above, iThera Medical developed commercial MSOT imaging systems, namely, 'MSOT inVision' which features 360° ring illumination, 270° acoustic detection, 10 fps and 150 µm spatial resolution [89–91].

For obtaining fluence-corrected PA imaging, Hussain et al. combined a PACT system with an acousto-optics (AO) tomography [59] by using a 64-element US array transducer (64 elements, 5 MHz central frequency, 100% bandwidth; Imasonic Inc., France) with a radius of curvature of 40 mm (Fig. 2d i). A commercially available clinical US system (MyLab One, ESAOTE, Italy) was used to transmit and acquire US and PA signals. A Nd:YAG laser was used to pump the optical parametric oscillator (680 to 910 nm, 6 ns pulse width; VersaScan L-532, Quantel, France) for PA illumination. The output laser was coupled into a custom-made multimode optical fiber bundle that splits main bundle into six smaller bundles to illuminate the imaging plane of the sample. The PA images were reconstructed using a filtered back-projection algorithm. For AO, an AO modulator was used to convert a single-mode continuous wave (CW) laser (Verdi 6, Coherent, USA) into a quasi-pulsed laser with a pulse width of 1.5 µs. Two CCD cameras were used to record the speckle pattern to measure ultrasonically modulated light. The sample was held stationary in the water tank for acoustic coupling. They performed experiments on phantoms, an ex-vivo tissue sample, and freshly sacrificed mice showing 2D PA images and fluence maps in a single instrument. They also demonstrated enhanced image after the fluence correction (Fig. 2d ii).

Tang et al. developed a miniature 3D wearable PACT (3D-wPAT) system to understand better the relationship between brain function and behavior [60]. They used miniaturized cap-shaped housing with a 3 × 64-element PVDF arc-shaped US array transducer (192 elements, 9.6 MHz central frequency, 100% bandwidth; Measurement Specialties, USA) (Fig. 2e i). The US array, arranged in a 2/3 annular case, could be mounted on a rat's head to keep its eyes from being blocked (Fig. 2e ii). An Nd:YAG pumped OPO laser (680–2550 nm, 10 ns pulse width, 20 Hz PRF; Continuum Inc., USA) was used to illuminate the target through a customized light delivery interface. A 192-channel preamplifier amplified the PA signals from the array transducer, then was 3:1 multiplexed into a 64-channel DAQ. Multiplexed PA signals were bandpass filtered (0.5–20 MHz) and reconstructed with a delay-and-sum beamforming algorithm. The in-plane resolution of this system was measured to be about 200 µm. They demonstrated the use of 3D-wPAT for monitoring sensory stimulus-evoked responses in behaving rats by measuring hemodynamic responses in the primary visual cortex during visual stimulation (Fig. 2e(iii)).

For assessing liver function reserve (LFR) in rabbits, Qiu et al. [61] introduced a PA imaging probe (Fig. 2f) based on their previous human study system [64]. A customized concave array (128 elements, 5 MHz central frequency, 90% bandwidth, 100 mm diameter, 172° spanning range; Japan Probe Co., Japan) was fully enclosed with a 100 µm PDMS film and filled up with deionized water (Fig. 2f(i)). The spatial resolutions of this system were about 1 mm (elevation) and 150 µm (cross-sectional). The illumination system contains a Q-switched Nd:YAG-pumped optical parameter oscillator system (Surelite, Continuum, USA) to support pulses at a wavelength ranging from 700 to 960 nm with 4 ns pulse width and 20 Hz PRF. An optic fiber bundle with a line-shaped illumination profile (40 mm × 10 mm) was set along side the the array transducer to provide lighting. A custom-built pre-amplifier was developed to amplify PA signals, and a 64-channel analog-to-digital system (National Instrument, USA) was used to receive amplified PA signals after 2:1 multiplexing. The signal was sampled at 12-bit digital resolution and at a sampling rate of 50 MS/s. The PA images were first reconstructed in real-time by using back-projection algorithm [35]. Using this system, they recorded in vivo ICG concentration change over time in a central auricular artery (CAA) of the rabbit's ear after ICG injection. The PA image of CAA (upper) and corresponding US image (lower) are shown in Fig. 2f(ii). Their results showed a distinct difference in ICG clearance between the control and partial hepatectomy models, thus demonstrating the clinical potential of PACT to evaluate in vivo LFR noninvasively.

Buehler et al. introduced a smaller size US array and applied it to human vasculature imaging [62] (Fig. 3a i).

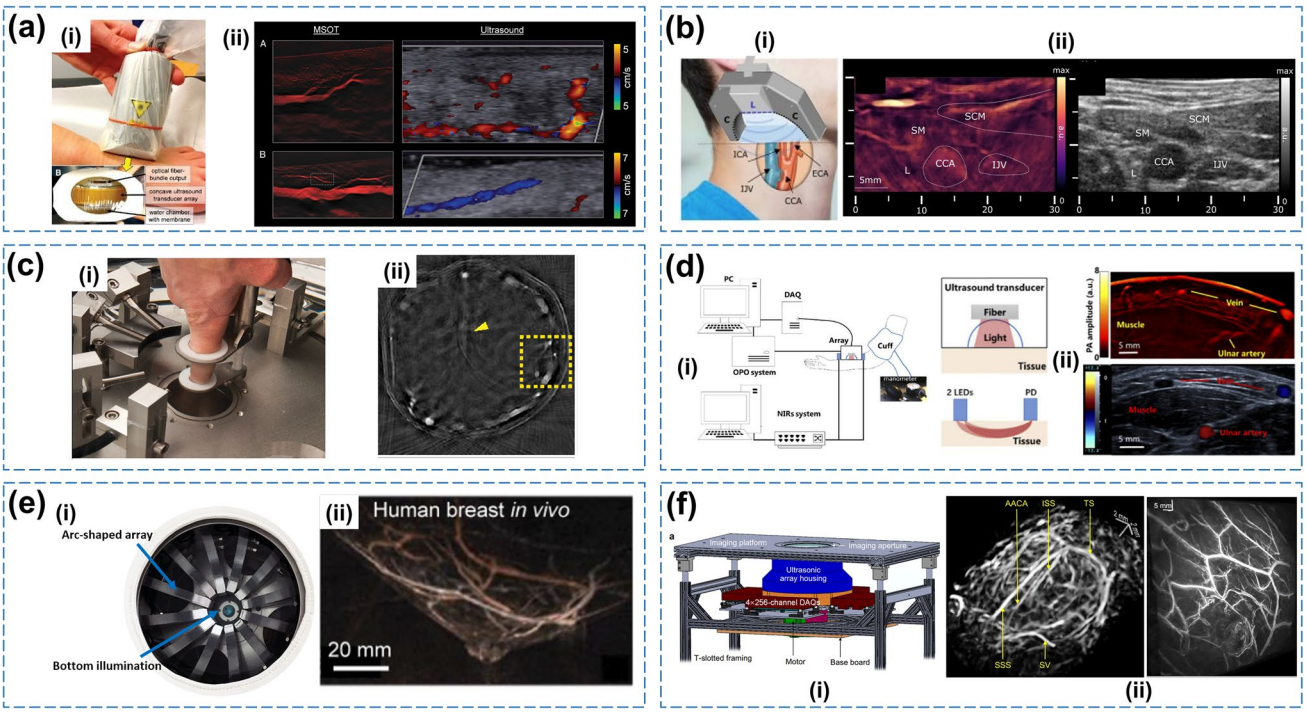


**Fig. 3** **a** (i) Handheld MSOT imaging probe [62]. (ii) Multispectral optoacoustic tomography images (left column) and duplex ultrasound images (right column) of small blood vessels. **b** (i) Geometry of the multi-modal (MSOT, pulse-echo US, and color Doppler) image acquisition with the multi-segment probe in transverse plane [92, 93]. ICA: internal carotid artery; ECA: external carotid artery; IJV: internal jugular vein; CCA: common carotid artery. (ii) Cross-sectional views of the left common carotid artery in the transverse plane. Left: PA image at 800 nm shows a clear identification of the common carotid artery and internal jugular vein. Right: Ultrasound image revealing the common carotid artery and jugular vein. **c** (i) Photograph of the PA computed tomography setup for human fingers [63]. (ii) PA cross-sectional images along the healthy index finger of a volunteer. **d** (i) Schematic of the PA tomography (PACT) system and near-infrared spectroscopy (NIR) system [65]. (ii) Cross-sectional PACT (above) and US (bottom) images of the human forearm. **e** (i) Schematic of Twente Photoacoustic Mammoscope 2 PA imaging system [66]. (ii) PA image of a sagittal view of the breast of a healthy volunteer. **f** (i) Schematic of high-speed 3D PACT system [67]. (ii) PA image of the whole rat brain (left) and the right breast of a healthy human subject (right). All images were reproduced with permission from. [62, 63, 65–67, 92, 93]

The array had 8 MHz central frequency, 128 elements with a focal length of 2 cm, and a view of 135°. The probe was sealed with an optically and acoustically transparent polyethylene plastic membrane, and it was filled with water for acoustic coupling. US gel was applied between membrane and skin to improve acoustic coupling and facilitate sliding of the transducer. They customized an optical parametric oscillator by diode-pumped Nd:YAG laser (InnoLas Laser GmbH, Krailing) with 680–980 nm tuning range, 50 Hz PRF, and 10 ns pulse width. Light from the laser was coupled into a fiber bundle. The output side of the bundle had a rectangular aperture to create an illumination zone of 2.5 mm × 12 mm (height × width) on the surface of the subject. They applied back-projection image reconstruction and spectral un-mixing algorithm and utilized a graphical processing unit (GPU) to enable real-time imaging [35]. The system could provide high-resolution images of the blood vessels in the foot down to 90 µm (FWHM), which were not visible in US color Doppler images (Fig. 3a ii).

Recently, to improve US image quality with a concave array, a multi-segment array transducer was developed [92, 93]. This array transducer (Imasonic SaS, Voray, France) has 60% bandwidth around 7.5 MHz. It consists of a central linear part (L) and two lateral concave (C) parts (Fig. 3b i). The linear part consists of 128 elements with 0.25 mm pitch while the two concave parts have 64 elements with their individual elements separated by a pitch of 0.6 mm. The concave part lies on a 40 mm radius arc and all their elements are cylindrically focused at a distance of 38 mm within the imaging plane. The elements of the linear segment are focused at 34 mm distance from the active aperture. For PA imaging, light illumination was provided using an optical parametric oscillator (OPO)-based laser (Innolas Laser GmbH, Krailling, Germany). The output beam was guided through a custom-made fiber bundle (Ceramoptec GmbH, Bonn, Germany). The PA signals collected by the array probe were digitized by a custom-made data acquisition system (Falkenstein Mikrosysteme GmbH, Taufkirchen, Germany) at a sampling rate of 40 MS/s. The linear array

part was used for US image formation by employing a synthetic transmit aperture (STA) focusing technique. US signal acquisition was performed by four 64-channel custom-built PCIe acquisition boards (S-Sharp Corporation, Taiwan). The in-plane resolutions were estimated to be about 250 µm and about 110 µm in US and PA imaging, respectively. They obtained the hybrid PA-US image along the common carotid artery from a healthy volunteer (Fig. 3b ii).

To investigate healthy human fingers and to image blood vessels across the interphalangeal joints, Peter et al. [63] presented a PACT based on a 32-element curvilinear US array (6.25 MHz central frequency, 80% bandwidth). The radius of curvature of the array was 40 mm, covered 85° of a circle (Fig. 3c i), and the in-plane resolution was about 100 µm. A 32-channel pulser/receiver with 80 MS/s sampling ratio was used for DAQ. Illumination uses an Nd:YAG laser (Quanta-Ray pro 250, Spectra Physics, Mountain View, California) pumping an optical parametric oscillator (VersaScan-L532, GWU, Erftstadt, Germany) at 10 Hz. The radial and angular positions of the fiber bundles were adjusted to achieve roughly equal-sized contiguous spots of 11 mm diameter on the skin surface. The pulse energy per fiber bundle was 6.5 mJ, giving an average fluence of 6.8 mJ/cm2 at the finger. The cross-sectional PA data of the healthy index finger were acquired using an 805 nm laser and by collecting 12 views with an angular step size of 30°. The total imaging time per slice with 20 signal averages was about one minute. The acquired data were reconstructed using an acoustic-filtered back-projection algorithm to generate the PA images [94]. The reconstructed slices across the proximal interphalangeal (PIP) joint (Fig. 3c ii) show rich detail of the blood vessels with diameters between 100 µm and 1.5 mm in various orientations and at multiple depths.

Yang et al. combined their previous PACT system [61, 64] with near-infrared spectroscopy (NIR) system to enable noninvasive visualization of the hemodynamic changes in forearm skeletal muscle during cuff occlusion in real-time (Fig. 3d i) [65]. The system is based on a 128-element concave array with 172° spanning range, 100 mm diameter, 5 MHz central frequency, and 90% bandwidth (Japan probe Co., Japan). The imaging probe contained the array transducer that was fully enclosed with a 100 µm polydimethylsiloxane (PDMS) film. The light illumination was provided by a tunable pulsed laser (Surelite OPO, Continuum, CA, USA) in the range of 680 to 960 nm. The pulse was up to 4 ns long, and the PRF was 20 Hz. A custom-built 128-channel preamplifier was connected to the probe, and the amplified PA signals were multiplexed 2:1 (PXIe5105, National Instrument, USA) and then transferred to a 64-channel 12-bit analog-to-digital system at a sampling rate of 50 MS/s. For the NIR part, two LEDs (780 nm and 840 nm) were employed to support continuous-wave light illumination. One photodiode detector was set to receive scattered light emerging from tissue. The source and detector were arranged in an elastic band at a distance of 2 cm attached to the arm. The DAQ system adopted a 16-channel, 16-bit DAQ card (PXIe-6358, National Instrument, USA) with a sampling rate of 1.25 MS/s, which was installed in the PXIe-1073 (National Instrument, USA) chassis to realize the communication between the acquisition card and the control host. They acquired high-resolution forearm skeletal muscle images along with corresponding US images (Fig. 3d ii). They observed hemodynamic changes during cuff occlusion with NIRS and showed a high correlation between NIRS results and PACT results.

For breast imaging, Schoustra et al. presented the Twente Photoacoustic Mammoscope 2 PA imaging system using 12 arc-shaped arrays [66]. Each array comprises 32 elements with 1 MHz central frequency and 100% bandwidth (Fig. 3e i). A dual-head laser (755 nm and 1064 nm) illuminates the breast with one beam directed at the nipple and nine other beams directed at the sides. PA signals were detected by 12 arc-shaped arrays curving along with the breast. The PA signals are acquired 12 times through 32-channel analog-to-digital converter as part of a DAQ system. Sampling is done with a 25 MHz sampling frequency and 14 bits. The imaging tank and the US arrays rotate around the breast in steps to obtain multiple projections. Three-dimensional images are reconstructed using a filtered back-projection algorithm. The breast image of one healthy volunteer showed breast contour, nipple, and the vascular anatomy within the breast (Fig. 3e ii).

Recently, Lin et al. developed a multipurpose 3D PACT imaging system to reveal angiographic information from the rodent brain to the human breast [67]. The system consists of (Fig. 3f i) US array housing, which has four arc-shaped US array transducers (2.25 MHz central frequency, 1024 elements, > 98% bandwidth; Imasonic, Inc., France) mounted on a hemispherical surface with a separation of 90°. Each arc-shaped array contains 256 transducer elements integrated on an 83° arc with a 130 mm radius. Each element had a flat-rectangular aperture with 0.6 mm × 0.7 mm size and 0.74 mm pitch. The US array housing was electrically grounded and was supported by eight metallic pillars that were fixed on an aluminum rotary board. By rotating the array by 90°, this system provided a large well-resolved FOV (diameter > 100 mm) and ~ $2\pi$ steradian solid angle with a nearly isotropic resolution of 370 to 390 µm. It took only 2 to 10 s to generate a volumetric image. The 1024-channel pre-amplification circuits with 51 dB gain were directly connected to the base of the US arrays' housing. The amplified PA signals were then transmitted to four DAQ modules via four customized phase plates (PhotoSound Inc., USA). Each DAQ module had 256-channel analog-to-digital converters (40 MHz maximum sampling rate; 12-bit dynamic range; ADC256, PhotoSound Inc., USA) and streamed the

digitized data to a solid-state drive via USB 3.0. The 1064-nm laser beam was directed to the subject from an Nd:YAG laser (10 Hz PRF, 8–12-ns pulse width; Quanta-Ray PRO-350–10, Spectra-Physics, USA) through the bottom of the hemispherical housing and expanded by two engineered diffusers. A Universal back-projection (UBP) algorithm [35] was used to reconstruct all images. They demonstrated in vivo imaging of rat brain showing angiographic anatomies and human breast within a single breath-hold (Fig. 3f ii). Later, this system was updated for human brain PACT imaging [95].

## 3 PACT systems based on ring-shaped array transducers

Arc-shaped arrays described in the previous sections solved the limited-view drawback of the linear US arrays to some extent. To overcome the limited-view limitations of 2D in-plane cross-section imaging, ring-shaped US array transducers are designed analogous to MRI and X-ray CT detection geometry [96–99] to accommodate round objects. The array encloses the illuminated area to receive PA waves along all in-plane directions to support high-quality images.

For small animal whole-body imaging, Xia et al. built a ring-shaped confocal PACT (RC-PACT) system [69] (Fig. 4a i). A custom-made 512-element full-ring array transducer (5 MHz central frequency, 80% bandwidth, 50 mm ring diameter) was used to receive PA signals. Each element in the array was shaped into an arc to produce an axial focal depth of 19 mm within the imaging plane. The combined foci of all elements generate a central imaging region of 20 mm diameter and 1 mm thickness. For achieving confocal laser beam illumination, a laser from a tunable Ti:Sapphire laser (12 ns pulse width, 10 Hz PRF) was first homogenized using an optical diffuser (EDC-5, RPC Photonics, USA) and then was passed through a conical lens (cone angle 130°; Delmar Photonics, USA) to form a ring-shaped light. The ring-shaped light was then focused using an optical condenser to project a light band around the animal. The thickness of the light band was 5 mm, and the cross-sectional diameter of the animal determined the diameter. The animal was held upright by a custom-built animal holder during the imaging. A 512 low-noise preamplifiers were used to amplify the transient PA waves measured around the sample. An 8:1 multiplexer on each receiver board selects one of eight channels and forwards the outputs to low-noise second-stage amplifiers, which is then received by a 64 channel DAQ system (40 MHz sampling frequency, 10-bit dynamic range). Images were reconstructed by a half-time image reconstruction algorithm. The system's tangential (transverse) and axial resolutions were 100–250 µm and 100 µm, respectively. In vivo RC-PACT images of athymic mice acquired at brain and trunk showed blood-rich organs, such as the eye (EY), cortical vessels (CV) on the brain and liver (LV), spinal cord (SC), and vena cava (VC) (Fig. 4a ii).

Elena et al. presented transmission-reflection optoacoustic ultrasound (TROPUS) computed tomography of small animals, which combines PACT with both transmission- and reflection-mode US-computed tomography (TUCT and

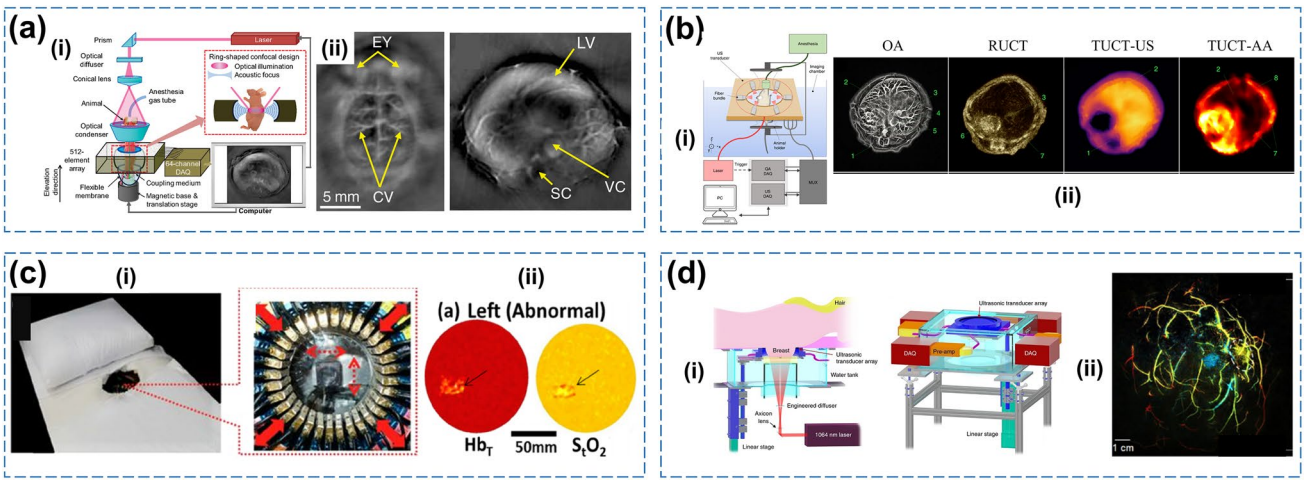


**Fig. 4** **a** (i) Schematic of the full-ring confocal whole-body photoacoustic computed tomography system [69]. (ii) In vivo PA images of athymic mice at the brain (left) and the liver (right). **b** (i) Schematic of the TROPUS system [70]. (ii) PA (OA, optoacoustic) image, reflection-mode ultrasound image, transmission-mode ultrasound images showing the distribution of the speed of sound and acoustic attenuation of the whole-body cross-section. **c** (i) Photographs of functional photoacoustic tomography clinical prototype [71]. (ii) Coronal $Hb_T$ and $S_tO_2$ maps of invasive mammary carcinoma in the left breast. **d** (i) Schematic of the single-breath-hold photoacoustic computed tomography [72]. (ii) PA image with color-encoded depths of a healthy breast. All images were reproduced with permission from. [69–72]

RUCT) [70] (Fig. 4b i). Small animals were surrounded by a ring array transducer consisting of two concave subarrays (256 elements, 174° active angular aperture, 5 MHz central frequency, 40 mm radius, 60% Tx/Rx bandwidth; Imasonic SaS, France). The laser illumination employed a 1064 nm pulsed Nd:YAG laser (9 mJ/cm$^2$, < 8 ns pulse width, 10 Hz PRF; Spectra-Physics, USA). They applied the synthetic transmit aperture (STA) technique, which activates sub-apertures of 128 elements for each transmission of only one element. For image reconstruction, the raw data were processed with a Butterworth bandpass filter and deconvolution with the electrical impulse response of the transducer. A weighted-based back-projection algorithm was implemented using TUCT results to reconstruct the image. To improve SNR, they detected in-plane motion artifacts using a retrospective motion correction algorithm, then averaged 35 to 50 frames, including 15 breathing frames, to remove motion artifacts. For enhancing contrast, contrast-limited adaptive histogram equalization (CLAHE) and a multiscale vesselness filter were applied. TROPUS system could obtain mapping information, including the absorbed optical energy, acoustic reflectivity, speed of sound, and acoustic attenuation, in whole live mice. Based on this information, they obtained whole-body in vivo mouse imaging using TUCT based speed of sound (TUCT-SoS) and TUCT based acoustic attenuation (TUCT-AA) (Fig. 4b ii).

Li et al. developed an fPACT to provide functional information on breast tissue [71]. The setup of the system lets the patient lie in the prone position with the breast pendant through an aperture in the patient bed (Fig. 4c i). A ring-shaped array was adjusted to fit the breast. The ring array consists of 64 elements, arranged in 2 rows of 32 elements (size of 2.3 mm × 30 mm), based on a polyvinylidene fluoride film (PVDF). The − 6-dB bandwidth of each transducer was from 380 to 1.48 MHz with a maximum frequency response of up to 2 MHz. For illuminating the whole breast, the light was delivered from the bottom of the table through a concave lens and ground glass. A large illumination area was achieved by scanning the whole breast in 2D using a light delivery system. The light source was a tunable pulsed Ti:Sapphire laser pumped with a Q-switched Nd:YAG laser (Symphotic Tii, Carmarillo, USA) and provides 8–25 ns pulse width at 10 Hz PRF. The beam was expanded to 6 cm$^2$ and diffused with ground glass to achieve a radiant exposure of 13 mJ/cm$^2$ at the breast surface. The transducers were connected to a 16-channel preamplifier and a 50 MHz 16-channel DAQ board via mechanical switching. They achieved multispectral image reconstruction by using a total variation minimization-based finite-element method to achieve deeper penetration depth. The functional characteristics used for fPACT diagnosis were calculated at the tumor sites (Fig. 4c ii).

Li et al. presented a single-breath-hold photoacoustic computed tomography (SBH-PACT) [72] based on their animal imaging system [73]. A patient could lie in a prone position on a patient bed with breast placed into a water tank through a hole in the table (Fig. 4d i). The detector around the breast was a 512 elements full-ring array (2.25 MHz central frequency, 110 mm radius, > 95% one-way bandwidth; Imasonic Inc., France). Four sets of 128-channel DAQ systems were used to capture data from all 512 elements. A 1064 nm laser (20 mJ/cm$^2$, 8–12 ns pulse width, 10 Hz PRF; Spectra-Physics, USA) light was incident in a donut-shaped beam to achieve uniform illumination inside the breast. The entire scan took 10 to 15 s for an SBH-PACT; thus, they could eliminate breathing-induced motion artifacts in post-processing. The image was reconstructed using the half-time UBP algorithm, and they added weight to the back-projected signals at different elevational divergence angles for 3D-UBP. The elevational resolution was 5.6 mm, and the in-plane resolution was 0.258 mm. They employed batch-processing and Hessian-based Frangi vesselness filtration To enhance the contrast in images. The maximum imaging depth achieved was 40 mm, measured in the cranial-caudal plane from the nipple toward the chest wall (Fig. 4d ii).

## 4 PACT systems based on hemispherical array transducers

The PACT is fundamentally a three dimensional imaging method because the illumination light generates 3D diffusive pattern PA signals from the illuminated target [3]. The ideal implementation of PACT needs a simultaneous collection of PA signals around the boundary of the imaging target to avoid limited-view effects and attain excellent image quality [3, 35]. To achieve this goal, researchers have developed various hemispherical array transducers which, have been used in both preclinical and clinical studies.

A new prototype PAI system (PAI-05) [74] equipped with a hemispherical detector array to image blood flow in limbs (Fig. 5a(i)) was developed by Kyoto University and Cannon Corporation based on their previous prototype PACT system (e.g., PAI-03, PAI-04) [75, 76]. The hemispherical array (Japan Probe Co., Japan) had 1024 elements on a 55-mm-radius hemisphere-shaped surface. The diameter of the single circular element was 2 mm with 3.35 MHz central frequency and over 85% bandwidth. The elements were arranged according to a 3D Fibonacci grid to attain uniform density. The DAQ system (Hitachi, Ltd., Japan) amplified the PA signal from 1024 channels at the time of light irradiation from the laser unit and sampled the received data at 60 MHz and 12 bits. The digital data were transferred to the PC for image reconstruction. The laser unit contains two laser systems (Lotis Tii Ltd., Belarus). Laser irradiated

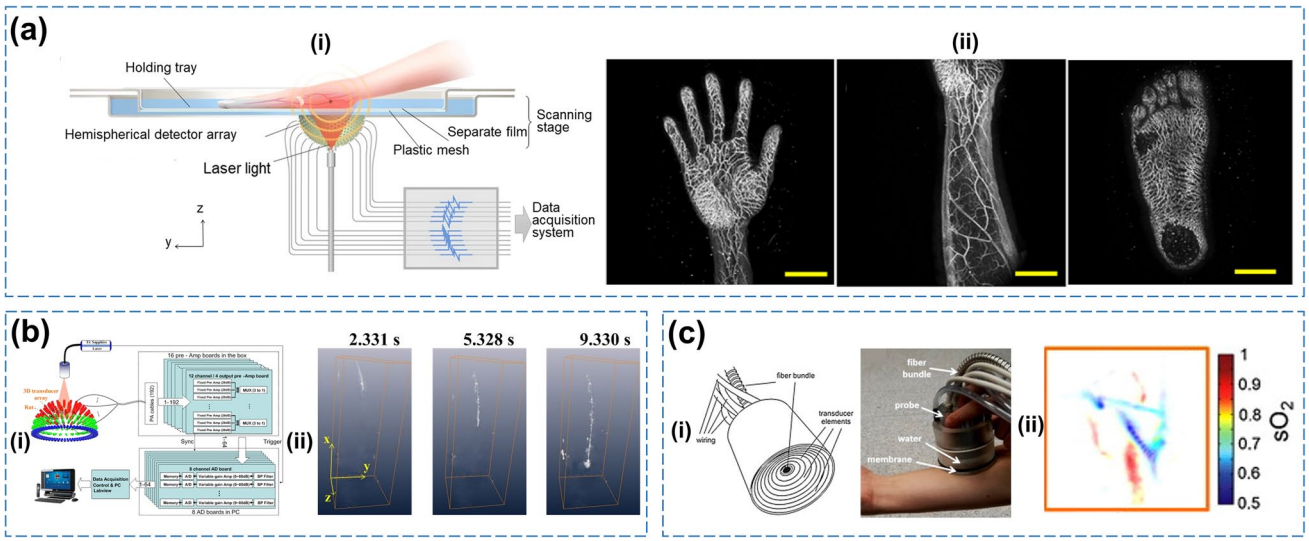


**Fig. 5** **a** (i) Schematic of the PAI-05 system configuration [74]. (ii) PA images of palm, forearm, and sole of the foot. **b** (i) Schematic of the 4D PACT system [77]. (ii) 3D PA guidance of a curved needle insertion and drug delivery in real-time. **c** (i) Layout and photograph of the clinical handheld vMSOT probe [78]. (ii) PA image of blood oxygen saturation of the wrist. All images were reproduced with permission from. [74, 77, 78]

light at 10 Hz PRF and wavelength could be selected from the range of 750 to 850 nm using a Ti:Sapphire laser and a Q-switched Nd:YAG laser. The wavelength could be set at steps of 1 nm. Alternate irradiation was performed using two different laser systems at every 50 ms. When two lasers were set to the same wavelength, they could irradiate at 20 Hz. UBP [35] was used for PA image reconstruction. The image reconstructions were realized in real-time by using pipeline data transfer and five graphics processing units (GPUs) (FirePro S9150, Advanced Micro Devices, Inc., USA). To establish the feasibility of imaging the human limbs using this system, they scanned several parts of the subject with an isotropic resolution of 0.21 mm (Fig. 5a ii). High-quality still images of a living human with a maximum FOV of 270 mm × 180 mm were obtained by scanning within the horizontal plane and then averaging the images.

Xiang et al. reported a 4D PACT, which integrates time resolution with a 3D by using spherical arrays of US detectors (Fig. 5b i) [77]. 192 elements were placed along a custom-fabricated white acyrlonitrile butadiene styrene spherical interface to create a 3D sphere array transducer. Each US detector has a 5 MHz central frequency and 70% nominal bandwidth with an active area of 3 mm in diameter and a total diameter of about 6 mm (Blatek, Inc., PA, USA). Excitation light originated from a tunable Ti:Sapphire laser (680 to 900 nm; Lotis Tii Ltd., Belarus), delivering < 6.5 ns pulse width with 10 Hz PRF. The beam was guided into a custom-made silica fused-end fiber bundle to create a cylindrical-shaped illumination pattern of approximately 20 mm in diameter on the surface of the imaged object. A 192 channel DAQ system consists of preamplifiers, secondary stage amplifiers for optimizing the SNR, and a 3:1 electronic multiplexer coupled with a 64-channel analog-to-digital converter. The average speed of PACT data acquisition was 0.33 s per frame and was limited by the 10 Hz PRF. The spatial resolution of this system was up to 0.19 mm in the xy-direction and up to 0.27 mm in the z-direction. PA images were reconstructed by using a 3D Spatial phase-controlled algorithm they proposed in the paper [50]. The 4D PACT system-generated motion pictures of imaged tissue, enabling real-time tracking of dynamic physiological and pathological processes at hundred micrometer-millisecond resolutions. It demonstrated real-time 3D images of PA-guided curved needle insertion (Fig. 5b ii).

A portable spherical array probe was first developed by Deán-Ben and Razansky for functional real-time PA imaging called vMSOT (volumetric multispectral optoacoustic tomography (vMSOT) [78]. This handheld array transducer consisted of 256 elements arranged on a spherical surface with a 40 mm radius and 90° solid angle (Imasonic SaS, France) (Fig. 5c i). Each element had a size of 3 mm × 3 mm, 4 MHz central frequency, and 100% available bandwidth. A silica fused-end fiber bundle (CeramOptics GmbH, Germany) was inserted into a hole at the center of the array for light delivery. The laser light beam was by a wavelength-tunable (690 to 900 nm) OPO laser (Phocus, Opotek Inc., USA) with short laser pulses (< 10 ns pulse width) and 10 Hz PRF. The cavity of the hemisphere was filled with water for acoustic coupling and sealed with a transparent polyethylene membrane. Raw PA signals from all elements were sampled at 40 MS/s using a custom-made 256-channel DAQ system (Falkenstein Mikrosysteme GmbH, Germany).

Fast volumetric PA images were reconstructed using GPU implementation of the 3D back-projection algorithm. The system had a relative isotropic resolution with 300 to 500 μm in the axial direction and 200 to 400 μm in the lateral direction. This system could visualize changes in the blood flow in real-time and could display multispectral tomographic reconstruction of the wrist region. A maximum amplitude projection (MAP) of blood oxygen saturation was calculated from images acquired at different wavelengths (Fig. 5c ii). Recently, this spherical array probe has been updated with flash scanning methods [100] and multi-beam illumination with wider angular coverage [101] thus offering outstanding capabilities for multiscale imaging of pharmacokinetics and biodistribution with high contrast, resolution, and speed.

## 5 Summary and future outlooks

PACT with a conventional linear array transducer is an intuitive and straightforward approach to building a dual model system with a US imaging system. However, PA images with linear array-based systems suffer from the limited-view area of the linear probes [4, 6], thus affecting the image quality. Three types of curved array transducers were developed for high-quality PA images to overcome this limited view shortcoming of the linear array. This paper summarizes the specifications of all these three types of curved array transducers with respect to ultrasound detection, light delivery, imaging performance, and reconstruction methods. The summary information is provided in Table 1.

The arc-shaped arrays were first developed and now have become the most widely used curved array transducer. The number of elements varies from 64–128, and the central frequency can be 8 or 9.6 MHz with about 100% bandwidth. With the handheld design, the minimum radius is 20 mm, similar to the linear array transducer in US imaging. Using the arc-shaped array, high PRF laser, and parallel DAQ system, 2D real-time display (B-scan) of up to 50 Hz [33, 40, 45] can be achieved without scanning. However, arc-shaped arrays still have the limited-view problem in the 2D case. To solve this problem, the ring-shaped array transducer is used in PACT as the ideal detection geometry in 2D case. It achieved better image qualities and large FOV 2D cross-sectional images with a diameter of 39 mm [72]. However, ring-shaped arrays still suffer from anisotropic spatial resolutions due to the difference between in-plane resolution and elevational resolution. New solutions comprising of hemispherical array transducers with a large FOV and real-time volumetric imaging with isotropic resolutions are being developed rapidly. The largest imaging area currently achieved using a hemispherical array with raster scanning is up to 270 mm × 180 mm [74].

Those three types of array transducers are widely used in preclinical and clinical research. For pre-clinical research, the arc-shaped and ring-shaped arrays offered cross-sectional imaging in real-time while volumetric imaging can be provided by the hemispherical array. All these arrays can be used for structural and functional imaging [55, 57, 59, 69, 102], monitoring organ perfusion [58, 61, 103], pharmacokinetics and bio-distribution [61, 100, 104], neuroimaging [60, 105, 106] and cancer research [89, 90]. The hemispherical transducer can directly provide 3D volumetric imaging while the arc-shaped array transducer should be rotated around the target to build a spherical detection geometry [57, 67] or scan the array along the elevation dimension [88] which reduced the temporal resolution of the system. The ring-shaped array can also provide 3D volumetric imaging by scanning the array along the elevation dimension [72] at the cost of temporal resolution. From this point of view, studies that need high temporal resolution in 3D like epileptic seizures [106] may only be achieved by the hemispherical.

For clinical research, high performance imaging of human subjects achieved by these three kinds of transducers including detecting breast lesions [66, 67, 71, 72, 75, 76], assessment of muscle [65, 107], bowel [108], thyroid [47, 64], peripheral vasculature [62–64, 74, 78, 93], and recently human brain [95]. Arc-shaped arrays were widely used since they can be easily compatible with traditional US imaging systems and for some special regions of the human body, such as the neck which are hard to achieve by other two kinds of array transducers. Ring-shaped array transducers cannot be optimized to all regions of the human body, so the application is limited to breast and peripheral vasculature. For a larger imaging area, such as the breast, the ring-shaped array and hemispherical array showed outstanding performance in clinical studies compared with the arc-shaped array with higher temporal resolution. Similar to pre-clinical application, the most significant advantage of using the hemispherical array is its ability to perform rapid volumetric imaging, which is crucial for studying certain dynamic physiological phenomena, such as visualizing blood oxygenation for diagnostic purposes [15].

The curved array transducers have been proposed to promote clinical translation and extend the fundamental applications of PACT with high-energy laser systems and novel scanning methods. However, several limitations still exist with these systems. First, the size of those array transducers (especially ring-shaped and hemispherical arrays) has now become much larger compared to linear arrays. Second, the transducer elements are opaque to light which means additional light paths should be considered for the system. Luckily, several groups are developing novel approaches to overcome these problems.

A typical piezoelectric-based US transducer consists of an active piezoelectric layer, single or multiple acoustic

**Table 1** Specifications of typical curved array based PACT system

| Platform | Ultrasound detection | | | | | Laser | | | | Imaging performance | | | | Reconstruction method | Applicaions |
|---|---|---|---|---|---|---|---|---|---|---|---|---|---|---|---|
| | Transducer type | # of elements | Center frequency (Bandwidth) | Radius | Scanning method | Wavelength | PRF | Light delivery | Pulse energy | Imaging speed/time | Imaging Depth | Resolution In plane (elevation) | Field of view / volume | | |
| Gamelin et al. [55, 56] | Arc Shaped | 128 | 5 MHz (80%) | 25 mm | Rotary scanning | 700-950 nm | 15 Hz | Free space | | 15 s | > 3 cm | 200 µm | | Delay-and-sum / Back-projection [35] | Mouse brain vasculature |
| Brecht et al. [57] | | 64 | 3.1 MHz (80%) | 65 mm | Rotary scanning | (1) 755 nm (2) 1064 nm | 10 Hz | Fiber bundle | 100 mJ | 8 min | | ~500 µm | 40 mm × 40 mm × 60 mm | Back projection | Mouse whole body imaging |
| Razansky et al. [58] | | 64 | 5 MHz (>50%) | 40 mm | Linear scanning | 680–950 nm | 10 Hz | Fiber bundle | 120 mJ | 10 Hz | | 150 µm / 800 µm | | Model-based method | Mouse whole body / Organ perfusion |
| Hussain et al. [59] | | 64 | 5 MHz (100%) | 40 mm | Rotary / Linear scanning | 680–910 nm | | Fiber bundle | | | 2–3 cm | 150 µm | | Filtered backprojection | Functional imaging |
| Tang et al. [60] | | 3 × 64 | 9.6 MHz (100%) | 36 mm | | 680–2550 nm | 50 Hz | Fiber bundle | | 3.33 Hz | 4-5 mm | 200 µm / >2 mm | 40 mm × 40 mm | Delay and sum | Neuroimage |
| Qiu et al. [61, 64] | | 128 | 5 MHz (90%) | 50 mm | | 700-960 nm | 20 Hz | Fiber bundle | | 10 Hz | 10 mm | 150 µm | 40 mm × 10 mm | Back-projection [35] | Pharmacokinetic and biodistribution |
| Buehler et al. [62] | | 128 | 8 MHz (60%) | 20 mm | | 680–980 nm | 50 Hz | Fiber bundle | | 50 Hz | 8 mm | 115 µm / 425 µm | 40 mm × 10 mm | Back-projection [35] | Human peripheral vasculature |
| Peter et al. [63] | | 32 | 6.25 MHz (80%) | 40 mm | Rotary scanning | 660–2550 nm | 10 Hz | Fiber bundle | 6.5 mJ (fiber output) | 1 min | | 100 µm | | Acoustic filtered backprojection [94] | Human peripheral vasculature |

**Table 1** (continued)

| Platform | Ultrasound detection | | | | | Laser | | | | Imaging performance | | | | Reconstruction method | Applicaions |
|---|---|---|---|---|---|---|---|---|---|---|---|---|---|---|---|
| | Transducer type | # of elements | Center frequency (Bandwidth) | Radius | Scanning method | Wavelength | PRF | Light delivery | Pulse energy | Imaging speed/time | Imaging Depth | Resolution In plane (elevation) | Field of view / volume | | |
| Yang et al. [61, 64, 65] | | 128 | 5 MHz (90%) | 50 mm | | 680–960 nm | 20 Hz | Fiber bundle | | 10 Hz | >2 cm | 150 µm | 40 mm × 20 mm | Back-projection [35] | Forearm muscle / Peripheral vasculature |
| Schoustra et al. [66] | | 12×32 | 1 MHz (100%) | 60 mm | Rotary scanning | (1) 755 nm (2) 1064 nm | 20 Hz | Free space/ Fiber bundles | 180 mJ | 4 min | 22 mm | 1.06 mm / 0.96 mm | 100 mm × 100 mm × 40 mm | Filtered backprojection | Human breast imaging |
| Lin et al. [67] | Arc Shaped | 1024 | 2.25 MHz (98%) | 130 mm | Rotary scanning | 1064 nm | 10 Hz | Free space | | 2-10 sec | 4 cm | 370-390 µm | ~140 mm × 140 mm × 40 mm | Universal backprojection [35] | Rat brain / Human breast |
| Deán-Ben et al. [92, 93] | Multi-segment arc-shaped | 128 | 7.5 MHz (70%) | 38 mm | | 680–980 nm | 25 Hz | Fiber bundle | 25 mJ | 25 Hz | >2 cm | 110 µm | 40 mm × 40mm | Back-projection[35] | Human-vasculature |
| Xia et al. [69] | Ring Shaped | 512 | 5 MHz (80%) | 50 mm | Linear scanning | 700–950 nm | 10 Hz | Free space | | 16 sec | | 250 µm | 20 mm (diameter) | Half-time image reconstruction | Mouse whole-body imaging |
| Elena et al. [70] | | 512 | 5 MHz (60%) | 40 mm | | 1064 nm | 10 Hz | Fiber bundle | ~54 mJ (fiber output) | 10 Hz | | ~200 µm | | Weighted-based back-projection | Mouse whole-body imaging |
| Li et al. [71] | | 64 | 0.93 MHz (> 100%) | | | | 10 Hz | Fiber bundles | | | | 500 µm | 6 $cm^2$ | Dual-mesh finite element method | Human breast imaging |
| Li et al. [72] | | 512 | 2.25 MHz (> 95%) | 110 mm | Linear scanning | 1064 nm | 10 Hz | Free space | | 10 Hz | | 258 µm / 5.6 mm | ~39 mm (diameter) | Half-time UBP algorithm | Human breast imaging |
| Nagae et al. [74] | Hemi-spherical | 1024 | 3.35 MHz (> 85%) | 55 mm | Spiral/ Raster scanning | 750–850 nm | 20 Hz | Free space | | 58-573 sec | 2 cm | 210 µm | 40 mm × 40 mm - 270 mm × 180 mm | Universal backprojection [35] | Human breast / Peripheral vasculature |

**Table 1** (continued)

| Platform | Ultrasound detection | | | | Laser | | | Imaging performance | | | | Recon-struction method | Applic-aions |
|---|---|---|---|---|---|---|---|---|---|---|---|---|---|
| | Transducer type | # of elements | Center frequency (Band-width) | Radius | Scanning method | Wave-length | PRF | Light delivery | Pulse energy | Imaging speed/time | Imaging Depth | Resolution In plane (eleva-tion) | Field of view / volume | | |
| Xiang et al. [77] | | 192 | 5 MHz (70%) | 70 mm | | 680–900 nm | 10 Hz | Fiber bundle | | 3 Hz | | 190 µm / 270 µm | π × 10 mm × 10 mm × 30 mm | 3-D SpatialNeedle phasec-ontrolled | insertion / Mouse brain |
| Deán-Ben et al. [78] | | 256 | 4 MHz | 40 mm | | 690–900 nm | 10 Hz | Fiber bundle | | 10 Hz | ~1 cm | 300-500 mm / 200-400 mm | 12 mm × 12 mm | Back-pro-jection algo-rithm | Human vascula-ture |

matching layers, backing, and an acoustic lens [113]. To make a transparent piezoelectric-based US transducer, researchers need to replace those layers above with transparent materials. Several piezoelectric-based transparent US transducers (TUT) with sufficient optical transmittance have been proposed recently [109, 114, 115]. Park et al. reported a transparent US transducer with lithium niobate (LNO) based TUT achieving 78% transparency at around 680 nm (Fig. 6a i). They seamlessly integrated US imaging, PA imaging, optical coherence tomography, and fluorescence imaging in one system [109]. Then they demonstrate the system's application in both ophthalmologic injuries and oncologic diseases (Fig. 6a ii).

Optical detection methods based on Fabry–Perot interferometer sensors [110, 116], micro-ring resonators [117, 118], and grating-based sensors [119] are also developed for PAI. Optical detection methods have a higher signal–noise ratio (SNR) per unit area, a wide frequency range and are less sensitive to electromagnetic [120]. Fabry-Pérot (FP) interferometers are transparent so they can be placed in contact with the sample and provide a tomographic view of the first few millimeters of mammalian tissue (Fig. 6b(i)) [120]. Plumb et al. showed peripheral arteries and microvascular vasomotor responses to thermal stimuli by using an FP transducer [110] (Fig. 6b ii).

Capacitive micromachined US transducers (CMUTs) are an alternative US array transducer for the PAI system. CMUT technology has compelling properties compared to piezoelectric transducers such as wide bandwidth and high receive sensitivity and higher acceptance angles [111, 113, 121]. Ilkhechi et al. introduced a transparent CMUT linear array with high transparency in the visible and near-infrared range (Fig. 6c i) [111]. The array transducer consists of 64 and 128 elements with immersion operation frequency of 8 MHz. PA images from gold wire phantom were achieved and provided lateral and axial resolutions of 234 µm and 220 µm (Fig. 6c ii).

Flexible and wearable electronics have attracted tremendous attention and are being developed rapidly in recent years [122]. Flexible US transducers have the advantages of lightweight structure and ultra-thin profile and can realize a conformal contact with curved and dynamic surfaces of skins [123]. Hu et al. reported a stretchable ultrasound probe that can confirm and detect nonplanar complex surfaces (Fig. 6d i) [112]. The wearable ultrasound device was ultrathin (240 µm) and stretchable. They reconstructed defects in 3D space with high spatial resolution through flat, concave, and convex surfaces (Fig. 6d ii).

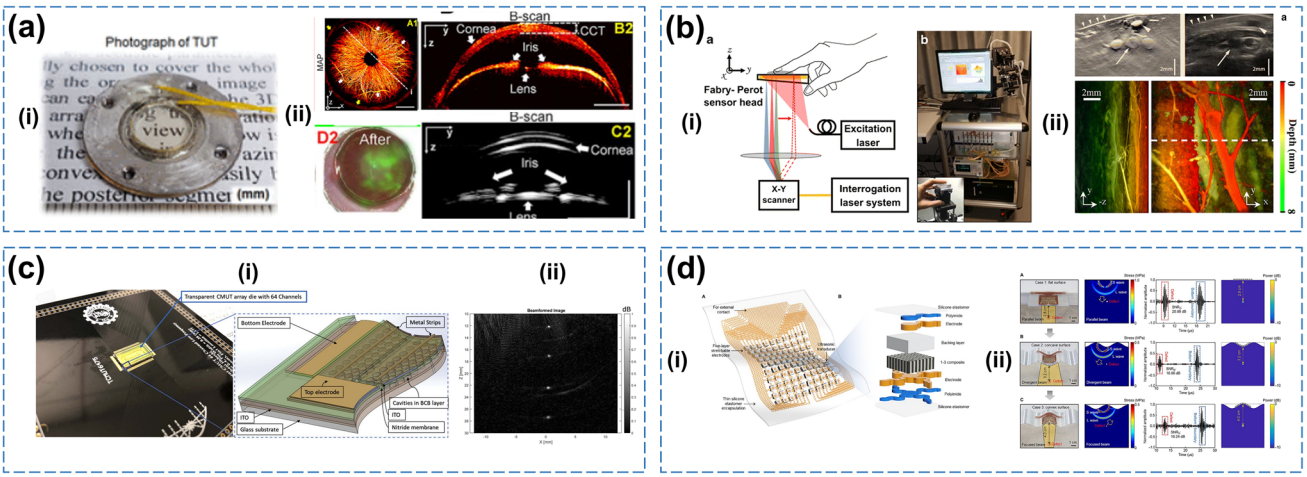


**Fig. 6** **a** Photograph of transparent US transducer-based lithium niobate [109]. (ii) In vivo quadruple fusion imaging of rats' eyes. **b** (i) A schematic and a photograph of Fabry–Perot PA imaging system setup [110]. (ii) 2D cross-sectional images of PA and US imaging, and coronal and sagittal maximum intensity projection volumetric PA images which are color-coded for depth. **c** (i) Wire bonded 64 channels transparent CMUT die on a PCB for testing and a 3D drawing of a transparent CMUT chip [111]. (ii) Reconstructed image of the PA data through the transducer. **d** (i) Schematics of the stretchable US transducer array and each component in an element [112]. (ii) A photo of experimental setups with the stretchable US device tested on complex surfaces, simulation results, pulse-echo signals from the boundaries and defects, and acquired 2D images. PA, photoacoustic; US, ultrasound; CMUT, capacitive micromachined ultrasound transducer. All images were reproduced with permission from. [109–112]

## 6 Conclusions

Photoacoustic imaging has become a promising biomedical imaging method in both pre-clinical and clinical studies. As one of the major implementations of PAI, PACT aims to reconstruct deeper targets with real-time display. The technological progress in ultrasound array transducers has provided a solid foundation for real-time 2D or 3D PACT in the past and continues to do so in the future. In this paper, we reviewed three representative PACT systems with respect to the shapes of array transducers to enhance the image quality of PACT. Since PA signals emit omnidirectionally, the linear US array used in US imaging suffers from a limited-view effect. Three types of curved array transducer discussed here, namely, arc-shaped, ring-shaped, and hemispherical, could obtain PA signals with a larger covering angle, resulting in improved image quality. While advantageous, many limitations remain in these approaches, as we discussed in the paper. The research field in PACT is very dynamic, and many groups are already investigating novel approaches to address these limitations with regard to the detector geometry and the acoustic sensors. By incorporating new advances from research communities, we believe the PACT technology could become a mainstream clinical tool for better health care in the near future.

**Acknowledgements** This research was supported in part by the Basic Science Research Program through the NRF funded by the Ministry of Education (2020R1A6A1A03047902), by the NRF grant funded by Ministry of Science and ICT (MSIT) (NRF-2019R1A2C2006269), by the Korea Medical Device Development Fund grant funded by the Korea government (the Ministry of Trade, Industry and Energy) (9991007019, KMDF_PR_20200901_0008), by the NRF grant funded by MSIT (2020M3H2A1078045), by a Global Ph.D. Fellowship Program of the NRF grant funded by the Ministry of Education (2019H1A2A1076500), and by the BK21 FOUR project.

### Declarations

**Conflict of interest** C. Kim has financial interests in OPTICHO, which, however, did not support this work.

**Human and animals rights** This article does not contain any studies with human participants or animals performed by any of the authors.

## References

1. Upputuri P, Pramanik M. Recent advances toward preclinical and clinical translation of photoacoustic tomography: a review. J Biomed Optic. 2016;22(4):041006.
2. Wang LV, Hu S. Photoacoustic tomography: in vivo imaging from organelles to organs. Science. 2012;335(6075):1458–62.
3. Taruttis A, Ntziachristos V. Advances in real-time multispectral optoacoustic imaging and its applications. Nat Photonics. 2015;9(4):219–27.
4. Choi W, Park E-Y, Jeon S, Kim C. Clinical photoacoustic imaging platforms. Biomed Eng Lett. 2018;8(2):139–55.
5. Das D, Sharma A, Rajendran P, Pramanik M. Another decade of photoacoustic imaging. Physics in Medicine & Biology. 2021;66(5):05TR1

6. Chen Q, Qin W, Qi W, Xi L. Progress of clinical translation of handheld and semi-handheld photoacoustic imaging. Photoacoustics. 2021;22:100264.
7. Yao J, Wang L. Perspective on fast-evolving photoacoustic tomography. J Biomed Optic. 2021;26(6):060602.
8. Wang LV, Yao J. A practical guide to photoacoustic tomography in the life sciences. Nat Methods. 2016;13(8):627–38.
9. Kim C, Jeon M, Wang LV. Nonionizing photoacoustic cystography in vivo. Opt Lett. 2011;36(18):3599–601.
10. Kim C, Favazza C, Wang LV. In vivo photoacoustic Tomography of chemicals: high-resolution functional and molecular optical imaging at new depths. Chem Rev. 2010;110(5):2756–82.
11. Hysi E, Fadhel MN, Moore MJ, Zalev J, Strohm EM, Kolios MC. Insights into photoacoustic speckle and applications in tumor characterization. Photoacoustics. 2019;14:37–48.
12. Baik JW, Kim H, Son M, Choi J, Kim KG, Baek JH, et al. Intraoperative Label-Free Photoacoustic histopathology of clinical specimens. laser & photonics Reviews.n/a(n/a):2100124
13. Ahn J, Kim JY, Choi W, Kim C. High-resolution functional photoacoustic monitoring of vascular dynamics in human fingers. Photoacoustics. 2021;23:100282.
14. Jeon M, Kim C. Multimodal photoacoustic tomography. IEEE Trans Multimed. 2013;15(5):975–82.
15. Schellenberg MW, Hunt HK. Hand-held optoacoustic imaging: a review. Photoacoustics. 2018;11:14–27.
16. Periyasamy V, Das N, Sharma A, Pramanik M. 1064 nm acoustic resolution photoacoustic microscopy. J Biophoton. 2019;12(5):e201800357.
17. Kim H, Baik JW, Jeon S, Kim JY, Kim C. PAExM: label-free hyper-resolution photoacoustic expansion microscopy. Opt Lett. 2020;45(24):6755–8.
18. Baik JW, Kim JY, Cho S, Choi S, Kim J, Kim C. Super Wide-field photoacoustic microscopy of animals and humans In Vivo. IEEE Trans Med Imag. 2020;39(4):975–84.
19. Kim J, Kim JY, Jeon S, Baik JW, Cho SH, Kim C. Super-resolution localization photoacoustic microscopy using intrinsic red blood cells as contrast absorbers. Light: Sci Appl. 2019;8(1):103.
20. Cho S, Baik J, Managuli R, Kim C. 3D PHOVIS: 3D photoacoustic visualization studio. Photoacoustics. 2020;18:100168.
21. Yao J, Wang L, Yang J-M, Maslov KI, Wong TTW, Li L, et al. High-speed label-free functional photoacoustic microscopy of mouse brain in action. Nat Methods. 2015;12(5):407–10.
22. Vu T, DiSpirito A, Li D, Wang Z, Zhu X, Chen M, et al. Deep image prior for undersampling high-speed photoacoustic microscopy. Photoacoustics. 2021;22:100266.
23. Liu C, Chen J, Zhang Y, Zhu J, Wang L. Five-wavelength optical-resolution photoacoustic microscopy of blood and lymphatic vessels. Adv Photon. 2021;3(1):016002.
24. Chen J, Zhang Y, He L, Liang Y, Wang L. Wide-field polygon-scanning photoacoustic microscopy of oxygen saturation at 1-MHz A-line rate. Photoacoustics. 2020;20:100195.
25. Li D, Liu C, Yang Y, Wang L, Shen Y. Micro-rocket robot with all-optic actuating and tracking in blood. Light: Sci Appl. 2020;9(1):84.
26. Liu C, Liang Y, Wang L. Optical-resolution photoacoustic microscopy of oxygen saturation with nonlinear compensation. Biomed Opt Exp. 2019;10(6):3061–9.
27. Kim JY, Lee C, Park K, Han S, Kim C. High-speed and high-SNR photoacoustic microscopy based on a galvanometer mirror in non-conducting liquid. Sci Rep. 2016;6(1):34803.
28. Vu T, Tang Y, Li M, Sankin G, Tang S, Chen S, et al. Photoacoustic computed tomography of mechanical HIFU-induced vascular injury. Biomed Opt Exp. 2021;12(9):5489–98.
29. Tang Y, Yao J. 3D Monte Carlo simulation of light distribution in mouse brain in quantitative photoacoustic computed tomography. Quant Imaging Med Surg. 2020;11(3):1046–59.
30. Wang D, Wang Y, Wang W, Luo D, Chitgupi U, Geng J, et al. Deep tissue photoacoustic computed tomography with a fast and compact laser system. Biomed Opt Exp. 2017;8(1):112–23.
31. Zheng W, Lee D, Xia J. Photoacoustic tomography of fingerprint and underlying vasculature for improved biometric identification. Sci Rep. 2021;11(1):17536.
32. Steinberg I, Kim J, Schneider MK, Hyun D, Zlitni A, Hopper SM, et al. Superiorized Photo-acoustic Non-NEgative reconstruction (SPANNER) for clinical photoacoustic imaging. IEEE Trans Med Imaging. 2021;40(7):1888–97.
33. Choi W, Oh D, Kim C. Practical photoacoustic tomography: Realistic limitations and technical solutions. J Appl Phys. 2020;127(23):230903.
34. Nyayapathi N, Zhang H, Zheng E, Nagarajan S, Bonaccio E, Takabe K, et al. Photoacoustic dual-scan mammoscope: results from 38 patients. Biomed Opt Exp. 2021;12(4):2054–63.
35. Xu M, Wang LV. Universal back-projection algorithm for photoacoustic computed tomography. Phys Rev E. 2005;71(1):016706.
36. Erpelding TN, Kim C, Pramanik M, Jankovic L, Maslov K, Guo Z, et al. Sentinel lymph nodes in the rat: noninvasive photoacoustic and US Imaging with a clinical US system. Radiology. 2010;256(1):102–10.
37. Neuschler EI, Butler R, Young CA, Barke LD, Bertrand ML, Böhm-Vélez M, et al. A pivotal study of optoacoustic imaging to diagnose benign and malignant breast masses: a new evaluation tool for radiologists. Radiology. 2018;287(2):398–412.
38. Garcia-Uribe A, Erpelding TN, Krumholz A, Ke H, Maslov K, Appleton C, et al. Dual-modality photoacoustic and ultrasound imaging system for noninvasive sentinel lymph node detection in patients with breast cancer. Sci Rep. 2015;5(1):15748.
39. Kim J, Park S, Jung Y, Chang S, Park J, Zhang Y, et al. Programmable real-time clinical photoacoustic and ultrasound imaging system. Sci Rep. 2016;6(1):35137.
40. Kim J, Park B, Ha J, Steinberg I, Hooper SM, Jeong C, et al. Multiparametric photoacoustic analysis of human thyroid cancers in vivo. Can Res. 2021;81(18):4849–60.
41. Choi C, Choi W, Kim J, Kim C. Non-invasive photothermal strain imaging of non-alcoholic fatty liver disease in live animals. IEEE Trans Med Imag. 2021;40(9):2487–95.
42. Park B, Bang CH, Lee C, Han JH, Choi W, Kim J, et al. 3D wide-field multispectral photoacoustic imaging of human melanomas in vivo: a pilot study. J Eur Acad Dermatol Venereol. 2021;35(3):669–76.
43. Lee C, Choi W, Kim J, Kim C. Three-dimensional clinical handheld photoacoustic/ultrasound scanner. Photoacoustics. 2020;18:100173.
44. Kim J, Park E-Y, Park B, Choi W, Lee KJ, Kim C. Towards clinical photoacoustic and ultrasound imaging: probe improvement and real-time graphical user interface. Exp Biol Med. 2020;245(4):321–9.
45. Jeon S, Park E-Y, Choi W, Managuli R, Kj L, Kim C. Real-time delay-multiply-and-sum beamforming with coherence factor for in vivo clinical photoacoustic imaging of humans. Photoacoustics. 2019;15:100136.
46. Kim J, Choi W, Park EY, Kang Y, Lee KJ, Kim HH, et al. Real-time photoacoustic thermometry combined with clinical ultrasound imaging and high-intensity focused ultrasound. IEEE Trans Biomed Eng. 2019;66(12):3330–8.
47. Cho S, Jeon S, Choi W, Managuli R, Kim C. Nonlinear pth root spectral magnitude scaling beamforming for clinical photoacoustic and ultrasound imaging. Opt Lett. 2020;45(16):4575–8.

48. Kim J, Kim YH, Park B, Seo H-M, Bang CH, Park GS, et al. Multispectral ex vivo photoacoustic imaging of cutaneous melanoma for better selection of the excision margin. Br J Dermatol. 2018;179(3):780–2.
49. Akers WJ, Edwards WB, Kim C, Xu B, Erpelding TN, Wang LV, et al. Multimodal sentinel lymph node mapping with single-photon emission computed tomography (SPECT)/computed tomography (CT) and photoacoustic tomography. Transl Res. 2012;159(3):175–81.
50. Sivasubramanian K, Pramanik M. High frame rate photoacoustic imaging at 7000 frames per second using clinical ultrasound system. Biomed Opt Exp. 2016;7(2):312–23.
51. Das D, Sivasubramanian K, Rajendran P, Pramanik M. Label-free high frame rate imaging of circulating blood clots using a dual modal ultrasound and photoacoustic system. J Biophoton. 2021;14(3):e202000371.
52. Li M, Vu T, Sankin G, Winship B, Boydston K, Terry R, et al. Internal-illumination photoacoustic tomography enhanced by a graded-scattering fiber diffuser. IEEE Trans Med Imag. 2021;40(1):346–56.
53. Nyayapathi N, Lim R, Zhang H, Zheng W, Wang Y, Tiao M, et al. Dual scan Mammoscope (DSM)—A new portable photoacoustic breast imaging system with scanning in craniocaudal plane. IEEE Trans Biomed Eng. 2020;67(5):1321–7.
54. Jeon S, Choi W, Park B, Kim C. A deep learning-based model that reduces speed of sound aberrations for improved in vivo photoacoustic imaging. IEEE Trans Image Process. 2021;30:8773–84.
55. Gamelin J, Aquirre A, Maurudis A, Huang F, Castillo D, Wang L, et al. Curved array photoacoustic tomographic system for small animal imaging. J Biomed Optic. 2008;13(2):024007.
56. Yang X, Maurudis A, Gamelin J, Aguirre A, Zhu Q, Wang L. Photoacoustic tomography of small animal brain with a curved array transducer. J Biomed Optic. 2009;14(5):054007.
57. Brecht H-P, Su R, Fronheiser M, Ermilov S, Conjusteau A, Oraevsky A. Whole-body three-dimensional optoacoustic tomography system for small animals. J Biomed Optic. 2009;14(6):064007.
58. Buehler A, Herzog E, Razansky D, Ntziachristos V. Video rate optoacoustic tomography of mouse kidney perfusion. Opt Lett. 2010;35(14):2475–7.
59. Hussain A, Hondebrink E, Staley J, Steenbergen W. Photoacoustic and acousto-optic tomography for quantitative and functional imaging. Optica. 2018;5(12):1579–89.
60. Tang J, Coleman JE, Dai X, Jiang H. Wearable 3-D photoacoustic tomography for functional brain imaging in behaving rats. Sci Rep. 2016;6(1):25470.
61. Qiu T, Yang J, Pan T, Peng C, Jiang H, Luo Y. Assessment of liver function reserve by photoacoustic tomography: a feasibility study. Biomed Opt Exp. 2020;11(7):3985–95.
62. Taruttis A, Timmermans AC, Wouters PC, Kacprowicz M, Dam GMv, Ntziachristo V. Optoacoustic imaging of human vasculature: feasibility by using a handheld probe. Radiology. 2016;281(1):256–63.
63. van Es P, Biswas S, Moens HJB, Steenbergen W, Manohar S. Initial results of finger imaging using photoacoustic computed tomography. J Biomed Optic. 2014;19(6):060501.
64. Yang J, Zhang G, Wu M, Shang Q, Huang L, Jiang H. Photoacoustic assessment of hemodynamic changes in foot vessels. J Biophoton. 2019;12(6):e201900004.
65. Yang J, Zhang G, Chang W, Chi Z, Shang Q, Wu M, et al. Photoacoustic imaging of hemodynamic changes in forearm skeletal muscle during cuff occlusion. Biomed Opt Exp. 2020;11(8):4560–70.
66. Schoustra S, Piras D, Huijink R, op't Root TJP, Alink L, Kobold WM, et al. Twente Photoacoustic Mammoscope 2: system overview and three-dimensional vascular network images in healthy breasts. J Biomed Optic 2019;24(12):121909
67. Lin L, Hu P, Tong X, Na S, Cao R, Yuan X, et al. High-speed three-dimensional photoacoustic computed tomography for preclinical research and clinical translation. Nat Commun. 2021;12(1):882.
68. Lee D, Park E-Y, Choi S, Kim H, Min J-j, Lee C, et al. GPU-accelerated 3D volumetric X-ray-induced acoustic computed tomography. Biomedical Optics Express. 2020;11(2):752–61
69. Xia J, Chatni M, Maslov K, Guo Z, Wang K, Anastasio M, et al. Whole-body ring-shaped confocal photoacoustic computed tomography of small animals in vivo. J Biomed Optic. 2012;17(5):050506.
70. Merčep E, Herraiz JL, Deán-Ben XL, Razansky D. Transmission–reflection optoacoustic ultrasound (TROPUS) computed tomography of small animals. Ligh:t Sci Appl. 2019;8(1):18.
71. Li X, Heldermon CD, Yao L, Xi L, Jiang H. High resolution functional photoacoustic tomography of breast cancer. Med Phys. 2015;42(9):5321–8.
72. Lin L, Hu P, Shi J, Appleton CM, Maslov K, Li L, et al. Single-breath-hold photoacoustic computed tomography of the breast. Nat Commun. 2018;9(1):2352.
73. Li L, Zhu L, Ma C, Lin L, Yao J, Wang L, et al. Single-impulse panoramic photoacoustic computed tomography of small-animal whole-body dynamics at high spatiotemporal resolution. Nat Biomed Eng. 2017;1(5):0071.
74. Nagae K, Asao Y, Sudo Y, Murayama N, Tanaka Y, Ohira K, et al. Real-time 3D photoacoustic visualization system with a wide field of view for imaging human limbs [version 2; peer review: 2 approved]. F1000Research. 2019;7(1813)
75. Toi M, Asao Y, Matsumoto Y, Sekiguchi H, Yoshikawa A, Takada M, et al. Visualization of tumor-related blood vessels in human breast by photoacoustic imaging system with a hemispherical detector array. Sci Rep. 2017;7(1):41970.
76. Matsumoto Y, Asao Y, Sekiguchi H, Yoshikawa A, Ishii T, Nagae K-i, et al. Visualising peripheral arterioles and venules through high-resolution and large-area photoacoustic imaging. Sci Rep. 2018;8(1):14930.
77. Xiang L, Wang B, Ji L, Jiang H. 4-D Photoacoustic tomography. Sci Rep. 2013;3(1):1113.
78. Deán-Ben XL, Razansky D. Functional optoacoustic human angiography with handheld video rate three dimensional scanner. Photoacoustics. 2013;1(3):68–73.
79. Yang C, Lan H, Gao F, Gao F. Review of deep learning for photoacoustic imaging. Photoacoustics. 2021;21:100215.
80. Na S, Wang LV. Photoacoustic computed tomography for functional human brain imaging [Invited]. Biomed Opt Express. 2021;12(7):4056–83.
81. Wang K, Li C, Chen R, Shi J. Recent advances in high-speed photoacoustic microscopy. Photoacoustics. 2021;24:100294.
82. Kuniyil Ajith Singh M, Xia W. Biomedical photoacoustic imaging and sensing using affordable resources. Sensors. 2021;21(7):2572.
83. Deng H, Qiao H, Dai Q, Ma C. Deep learning in photoacoustic imaging: a review. J Biomed Opt. 2021;26(4):040901.
84. Cho S-W, Park SM, Park B, Kim DY, Lee TG, Kim B-M, et al. High-speed photoacoustic microscopy: a review dedicated on light sources. Photoacoustics. 2021;24:100291.
85. Yang X, Chen Y-H, Xia F, Sawan M. Photoacoustic imaging for monitoring of stroke diseases: a review. Photoacoustics. 2021;23:100287.
86. Dima A, Burton NC, Ntziachristos V. Multispectral optoacoustic tomography at 64, 128, and 256 channels. J Biomed Opt. 2014;19(3):36021.

87. Buehler A, Kacprowicz M, Taruttis A, Ntziachristos V. Real-time handheld multispectral optoacoustic imaging. Opt Lett. 2013;38(9):1404–6.
88. Olefir I, Merčep E, Burton N, Ovsepian S, Ntziachristos V. Hybrid multispectral optoacoustic and ultrasound tomography for morphological and physiological brain imaging. J Biomed Optic. 2016;21(8):086005.
89. Tomaszewski MR, Gonzalez IQ, O'Connor JP, Abeyakoon O, Parker GJ, Williams KJ, et al. Oxygen enhanced optoacoustic tomography (OE-OT) reveals vascular dynamics in murine models of prostate cancer. Theranostics. 2017;7(11):2900–13.
90. Gehrung M, Tomaszewski M, McIntyre D, Disselhorst J, Bohndiek S. Co-registration of optoacoustic tomography and magnetic resonance imaging data from murine tumour models. Photoacoustics. 2020;18:100147.
91. Qi L, Wu J, Li X, Zhang S, Huang S, Feng Q, et al. Photoacoustic Tomography image restoration with measured spatially variant point spread functions. IEEE Trans Med Imag. 2021;40(9):2318–28.
92. Deán-Ben XL, Merčep E, Razansky D. Hybrid-array-based optoacoustic and ultrasound (OPUS) imaging of biological tissues. Appl Phys Lett. 2017;110(20):203703.
93. Merčep E, Deán-Ben XL, Razansky D. Imaging of blood flow and oxygen state with a multi-segment optoacoustic ultrasound array. Photoacoustics. 2018;10:48–53.
94. Jose J, Willemink RGH, Steenbergen W, Slump CH, van Leeuwen TG, Manohar S. Speed-of-sound compensated photoacoustic tomography for accurate imaging. Med Phys. 2012;39(12):7262–71.
95. Na S, Russin JJ, Lin L, Yuan X, Hu P, Jann KB, et al. Massively parallel functional photoacoustic computed tomography of the human brain. Nature Biomedical Engineering. 2021
96. Xia J, Wang LV. Small-animal whole-body photoacoustic tomography: a review. IEEE Trans Biomed Eng. 2014;61(5):1380–9.
97. Kanchana R, Menaka R. Ischemic stroke lesion detection, characterization and classification in CT images with optimal features selection. Biomed Eng Lett. 2020;10(3):333–44.
98. Hegazy MAA, Cho MH, Cho MH, Lee SY. U-net based metal segmentation on projection domain for metal artifact reduction in dental CT. Biomed Eng Lett. 2019;9(3):375–85.
99. Comelli A, Dahiya N, Stefano A, Benfante V, Gentile G, Agnese V, et al. Deep learning approach for the segmentation of aneurysmal ascending aorta. Biomed Eng Lett. 2021;11(1):15–24.
100. Ron A, Kalva SK, Periyasamy V, Deán-Ben XL, Razansky D. Flash scanning volumetric optoacoustic tomography for high resolution whole-body tracking of nanoagent kinetics and biodistribution. Laser Photon Rev. 2021;15(3):2000484.
101. Kalva SK, Dean-Ben XL, Razansky D. Single-sweep volumetric optoacoustic tomography of whole mice. Photon Res. 2021;9(6):899–908.
102. Zhang Y, Wang L. Video-rate ring-array ultrasound and photoacoustic tomography. IEEE Trans Med Imag. 2020;39(12):4369–75.
103. Deán-Ben XL, Fehm TF, Ford SJ, Gottschalk S, Razansky D. Spiral volumetric optoacoustic tomography visualizes multiscale dynamics in mice. Light: Sci Appl. 2017;6(4):16247.
104. Gurka MK, Pender D, Chuong P, Fouts BL, Sobelov A, McNally MW, et al. Identification of pancreatic tumors in vivo with ligand-targeted, pH responsive mesoporous silica nanoparticles by multispectral optoacoustic tomography. J Control Release. 2016;231:60–7.
105. Nasiriavanaki M, Xia J, Wan H, Bauer AQ, Culver JP, Wang LV. High-resolution photoacoustic tomography of resting-state functional connectivity in the mouse brain. Proc Natl Acad Sci. 2014;111(1):21–6.
106. Gottschalk S, Fehm T, Deán-Ben XL, Tsytsarev V, Razansky D. Correlation between volumetric oxygenation responses and electrophysiology identifies deep thalamocortical activity during epileptic seizures. Neurophotonics. 2016;4(1):011007.
107. Regensburger AP, Fonteyne LM, Jüngert J, Wagner AL, Gerhalter T, Nagel AM, et al. Detection of collagens by multispectral optoacoustic tomography as an imaging biomarker for Duchenne muscular dystrophy. Nat Med. 2019;25(12):1905–15.
108. Knieling F, Neufert C, Hartmann A, Claussen J, Urich A, Egger C, et al. Multispectral optoacoustic tomography for assessment of Crohn's disease activity. N Engl J Med. 2017;376(13):1292–4.
109. Park J, Park B, Kim TY, Jung S, Choi WJ, Ahn J, et al. Quadruple ultrasound, photoacoustic, optical coherence, and fluorescence fusion imaging with a transparent ultrasound transducer. Proceed Natl Acad Sci. 2021;118(11):e1920879118.
110. Plumb AA, Huynh NT, Guggenheim J, Zhang E, Beard P. Rapid volumetric photoacoustic tomographic imaging with a Fabry-Perot ultrasound sensor depicts peripheral arteries and microvascular vasomotor responses to thermal stimuli. Eur Radiol. 2018;28(3):1037–45.
111. Ilkhechi AK, Ceroici C, Li Z, Zemp R. Transparent capacitive micromachined ultrasonic transducer (CMUT) arrays for real-time photoacoustic applications. Opt Exp. 2020;28(9):13750–60.
112. Hu H, Zhu X, Wang C, Zhang L, Li X, Lee S, et al. Stretchable ultrasonic transducer arrays for three-dimensional imaging on complex surfaces. Sci Adv. 2018;4(3):eaar3979.
113. Ren D, Sun Y, Shi J, Chen R. A review of transparent sensors for photoacoustic imaging applications. Photonics. 2021;8(8):324.
114. Chen R, He Y, Shi J, Yung C, Hwang J, Wang LV, et al. Transparent High-Frequency Ultrasonic Transducer for Photoacoustic Microscopy Application. IEEE Trans Ultrason Ferroelectr Freq Control. 2020;67(9):1848–53.
115. Park B, Han M, Park J, Kim T, Ryu H, Seo Y, et al. A photoacoustic finder fully integrated with a solid-state dye laser and transparent ultrasound transducer. Photoacoustics. 2021;23:100290.
116. Zhang E, Laufer J, Beard P. Backward-mode multiwavelength photoacoustic scanner using a planar Fabry-Perot polymer film ultrasound sensor for high-resolution three-dimensional imaging of biological tissues. Appl Opt. 2008;47(4):561–77.
117. Dong B, Li H, Zhang Z, Zhang K, Chen S, Sun C, et al. Isometric multimodal photoacoustic microscopy based on optically transparent micro-ring ultrasonic detection. Optica. 2015;2(2):169–76.
118. Li H, Dong B, Zhang Z, Zhang HF, Sun C. A transparent broadband ultrasonic detector based on an optical micro-ring resonator for photoacoustic microscopy. Sci Rep. 2014;4(1):4496.
119. Shnaiderman R, Wissmeyer G, Ülgen O, Mustafa Q, Chmyrov A, Ntziachristos V. A submicrometre silicon-on-insulator resonator for ultrasound detection. Nature. 2020;585(7825):372–8.
120. Wissmeyer G, Pleitez MA, Rosenthal A, Ntziachristos V. Looking at sound: optoacoustics with all-optical ultrasound detection. Light: Sci Appl. 2018;7(1):53.
121. Manwar R, Kratkiewicz K, Avanaki K. Overview of ultrasound detection technologies for photoacoustic imaging. Micromachines. 2020;11(7):692.
122. Hua Q, Sun J, Liu H, Bao R, Yu R, Zhai J, et al. Skin-inspired highly stretchable and conformable matrix networks for multifunctional sensing. Nat Commun. 2018;9(1):244.
123. Liu W, Zhu C, Wu D. Flexible and stretchable ultrasonic transducer array conformed to complex surfaces. IEEE Electron Device Lett. 2021;42(2):240–3.